PCCP

ROYAL SOCIETY OF CHEMISTRY

PAPER

View Article Online
View Journal | View Issue

Check for updates

Cite this: *Phys. Chem. Chem. Phys.*, 2022, **24**, 11222

Microsolvation of H_2O^+, H_3O^+, and $CH_3OH_2^+$ by He in a cryogenic ion trap: structure of solvation shells†

David Müller and Otto Dopfer *

Due to the weak interactions of He atoms with neutral molecules and ions, the preparation of size-selected clusters for the spectroscopic characterization of their structures, energies, and large amplitude motions is a challenging task. Herein, we generate $H_2O^+He_n$ ($n \leq 9$) and $H_3O^+He_n$ ($n \leq 5$) clusters by stepwise addition of He atoms to mass-selected ions stored in a cryogenic 22-pole ion trap held at 5 K. The population of the clusters as a function of n provides insight into the structure of the first He solvation shell around these ions given by the anisotropy of the cation–He interaction potential. To rationalize the observed cluster size distributions, the structural, energetic, and vibrational properties of the clusters are characterized by *ab initio* calculations up to the CCSD(T)/aug-cc-pVTZ level. The cluster growth around both the open-shell H_2O^+ and closed-shell H_3O^+ ions begins by forming nearly linear and equivalent OH···He hydrogen bonds (H-bonds) leading to symmetric structures. The strength of these H-bonds decreases slightly with n due to noncooperative three-body induction forces and is weaker for H_3O^+ than for H_2O^+ due to both enhanced charge delocalization and reduced acidity of the OH protons. After filling all available H-bonded sites, addition of further He ligands around H_2O^+ (n = 3–4) occurs at the electrophilic singly occupied $2p_z$ orbital of O leading to O···He p-bonds stabilized by induction and small charge transfer from H_2O^+ to He. As this orbital is filled for H_3O^+, He atoms occupy in the n = 4–6 clusters positions between the H-bonded He atoms, leading to a slightly distorted regular hexagon ring for n = 6. Comparison between $H_3O^+He_n$ and $CH_3OH_2^+He_n$ illustrates that CH_3 substitution substantially reduces the acidity of the OH protons, so that only clusters up to n = 2 can be observed. The structure of the solvation sub-shells is visible in both the binding energies and the predicted vibrational OH stretch and bend frequencies.

Received 11th March 2022,
Accepted 20th April 2022

DOI: 10.1039/d2cp01192a

rsc.li/pccp

Open Access Article. Published on 20 April 2022. Downloaded on 12/31/2025 2:24:13 PM.
This article is licensed under a Creative Commons Attribution 3.0 Unported Licence.

1. Introduction

The weak interaction of He with neutral and charged atoms and molecules is relevant for several disciplines, including molecular physics, low-temperature physics and chemistry, plasma chemistry, and astrochemistry. He atoms are quantum objects and their neutral clusters serve as models to investigate superfluidity and large-amplitude motion at the molecular level.[1–8] In general, the interaction of He with cations is stronger than for neutrals due to additional electrostatic and induction forces arising from the excess positive charge, leading to deeper potential wells and larger angular anisotropy of the interaction potential.[9–11] For some closed-shell and open-shell cations strong chemical bonds may be formed (*e.g.*, H^+He, He_2^+).[9] In the case of noncovalent X^+He_n clusters, their low binding energy makes their efficient production for spectroscopic characterization a challenging task.

Pioneering experiments of X^+He_n clusters were carried out by Kobayashi and coworkers,[12–14] who injected X^+ ions into drift tubes cooled by liquid He and filled with rarified He gas to generate and characterize these clusters by mass spectrometry, thereby revealing initial experimental information about their stability and structure (magic numbers). Since then, three major approaches have been applied as efficient X^+He_n ion sources. In the first bottom-up approach developed around three decades ago, X^+He_n clusters are generated in supersonic plasma expansions in which X^+ ions are generated by electron or chemical ionization or laser desorption. The cold clusters generated can readily be characterized by infrared or optical photodissociation (IRPD, UV/visPD).[10,15,16] One of the early visPD examples includes N_2^+ ($n \leq 3$) with free internal rotation of the He atoms around the N_2^+ rod.[17] IRPD studies of small closed-shell and open-shell protonated X^+ ions include HCO^+

Institut für Optik und Atomare Physik, Technische Universität Berlin, Hardenbergstr. 36, 10623 Berlin, Germany. E-mail: dopfer@physik.tu-berlin.de

† Electronic supplementary information (ESI) available. See DOI: https://doi.org/10.1039/d2cp01192a

This journal is © the Owner Societies 2022

Open Access Article. Published on 20 April 2022. Downloaded on 12/31/2025 2:24:13 PM.
This article is licensed under a Creative Commons Attribution 3.0 Unported Licence.

(n = 1),[18] HN_2^+ ($n \leq 2$),[19] NH_2^+ (n = 1),[20] NH_4^+ (n = 1),[21,22] OH^+ (n = 1),[23] H_2O^+ (n = 1),[24] HO_2^+ (n = 1),[25] HCO_2^+ (n = 1), CH_3^+ (n = 1),[15,26,27] $SiOH^+$ (n = 1),[28] but also large aromatic and cycloalkane ions, such as phenol$^+$ (n = 1),[29] acetanilide$^+$ (n = 1),[30] and adamantane$^+$ ($n \leq 3$).[31] However, it is often difficult to attach more than one He atom to the X^+ cation as substantial energy has to be injected into the expansion to generate the ions and the expansion provides a too short time and pressure window to grow cold X^+He_n clusters with larger n.

A second bottom-up approach developed later by Asmis and coworkers is growing X^+He_n ions in a cryogenic trap.[32–35] In this approach, ions are prepared in an arbitrary ion source, mass-selected, and trapped in a cryogenic trap by He buffer gas cooling. During the cooling process, larger X^+He_n clusters can be formed and the limit of n is mostly given by the He binding energy and the cooling efficiency of the trap. As a result of the longer time for cluster growth, often larger X^+He_n clusters can be formed in the trap than in the plasma expansion. This approach has been widely adopted by several groups to form X^+He_n clusters around smaller and larger cations,[34,36–40] such as inorganic and small hydrocarbon ions,[8,35,41–46] C_{60}^+,[47–49] and protonated PAH (coronene)[50] and biomolecules,[35,39] as well as reaction intermediates.[38] However, in many of these studies, He-tagging is barely used for spectroscopy of the bare X^+ ion and no or only little attention has been paid to the $X^+\cdots$He interaction potential. Because of the larger binding energies, in most cases larger rare gas atoms, H_2, or N_2 are used as a tag in spectroscopy experiments coupled to cryogenic traps.

A third and top-down approach to generate X^+He_n clusters is ionization of doped helium nanodroplets, $X@He_m$. Briefly, in this technique one or more neutral atoms or molecules are picked up by very large He_m clusters ($m = 10^3$–10^7) and then ionized typically by electron impact. As a result of the excess ionization energy, most He atoms evaporate. The remaining population of the small X^+He_n products ($n \ll m$) may be analysed by mass spectrometry to reveal magic numbers and structures of solvation shells or used for photodissociation spectroscopy. This technique has been pioneered and extensively applied by Scheier and his group to a plethora of cations,[51,52] including metal, PAH, and fullerene cations and their clusters.[53–58] Few groups have also started recently to perform elegant ion spectroscopy in large He droplets,[59–67] although this approach does not provide details about the local $X^+\cdots$He interaction potential (radial strength and angular anisotropy).

Herein, we report the generation of $H_2O^+He_n$ and $H_3O^+He_n$ clusters in our recently commissioned cryogenic ion trap coupled to a quadrupole/time-of-flight tandem mass spectrometer (BerlinTrap).[68] As we use this bottom-up approach for X^+He_n generation in this tandem mass spectrometer combination for the first time, we describe the instrument-specific data analysis in some detail and validate the approach for $CH_3^+He_n$ and $H_3O^+He_n$, for which corresponding cluster growth experiments have been performed before in a quadrupole/quadrupole tandem mass spectrometer.[34,42] The $H_2O^+He_n$ clusters are grown for the first time and extend our previous IRPD work on H_2O^+He (n = 1), in which we could produce in a plasma expansion not enough larger clusters for spectroscopic interrogation.[24] In that work, high-resolution rotation–vibration-tunneling spectroscopy has been performed for H_2O^+He and partly deuterated species, providing precise information about the 3D interaction potential by comparison to *ab initio* calculations at the MP2/aug-cc-pVTZ level. No spectroscopic information appears to be available for $H_2O^+He_{n\geq 2}$ and any of the $H_3O^+He_n$ clusters. To this end, we employ in the present work CCSD and CCSD(T) calculations to determine the structural, energetic, and vibrational properties of $H_2O^+He_{n\leq 5}$ and $H_3O^+He_{n\leq 6}$ for investigating the solvation shell structure and for preparation of future IRPD experiments in the BerlinTrap. For comparison to $H_3O^+He_n$, we investigate also $CH_3OH_2^{+\cdot}He_{n\leq 2}$ clusters[43] using the same experimental and computational strategy to extract the effects of H → CH_3 substitution on the $X^+\cdots$He interaction potential. Complexes of small interstellar hydroxy cations with He, such as OH^+,[69] H_2O^+,[70] and H_3O^+,[71] are of special interest in the context of astrophysics and considered in several models of astrochemistry.[72]

2. Experimental and computational techniques

The cluster growth experiments are carried out in an ion-trap quadrupole/time-of-flight tandem mass spectrometer (BerlinTrap) described in detail elsewhere.[68,73] Briefly, it consists of an ion source for ion generation, a quadrupole mass spectrometer (QPMS) for ion selection, an electrostatic bender for ion deflection, an octupole ion guide for transferring the ions into a cryogenic 22-pole ion trap used for trapping and cooling the ions *via* He buffer gas (purity 5.0, Air Liquide, impurities O_2 and H_2O < 3 ppm), an Einzel lens stack for focusing the ions, and finally a reflectron time-of-flight (ReTOF) mass spectrometer for detecting the product ions. For the current study, the original electrospray ionization (ESI) source is used to produce the closed-shell ions H_3O^+, CH_3^+, and $CH_3OH_2^+$,[68] while for the open-shell H_2O^+ ions the ESI source is replaced by an electron ionization (EI) source.[73] H_3O^+ and $CH_3OH_2^+$ are readily produced by ESI of solutions containing H_2O or CH_3OH with some addition of acetic acid. CH_3^+ is a major fragment of $CH_3OH_2^+$ by elimination of H_2O. The H_2O^+ cations are produced by standard electron ionization of H_2O using electrons with a kinetic energy of typically 70 eV. The X^+ ions generated by ESI or EI are mass-selected by the QPMS and injected in the 22-pole trap held at 5 K by a cryostat. The ions are then trapped and cooled down by an intense He pulse injected into the trap just before the ions enter the trap. Spectroscopic analysis of hot band intensities in the electronic spectra of a variety of biomolecular ions yield an effective vibrational temperature in the range of 15–30 K for trap temperatures of 4–6 K, illustrating that the ion temperature does not fully reach the trap temperature.[68,74–76] During this process, X^+He_n clusters grow in the trap. The resulting X^+He_n cluster distribution is extracted into the extraction region of an orthogonal ReTOF (with a resolution of $m/\Delta m > 100$ in the

Open Access Article. Published on 20 April 2022. Downloaded on 12/31/2025 2:24:13 PM.
This article is licensed under a Creative Commons Attribution 3.0 Unported Licence.

considered size range) where they are accelerated by a high voltage pulse toward a dual stage microchannel plate detector in Chevron arrangement.

One particular feature of the BerlinTrap setup is the distance between the 22-pole trap and the ReTOF (*ca.* 0.5 m), which acts as additional time-of-flight discriminator and leads to variable transmission efficiencies for ions with different masses *via* the choice of the delay between the 22-pole extraction and the ReTOF extraction. To compensate for this effect, mass spectra are recorded at varying delay times in steps of typically 2 μs and added up to cover the whole X^+He_n cluster distribution. Fig. 1 illustrates this procedure for the case of $H_3O^+He_n$ clusters for selected delay times and the sum spectrum.[68] As can be seen, for early extraction at 60 μs delay only $H_3O^+He_n$ with n = 0–2 have significant transmission. On the other hand, at late extraction at 74 μs delay only n = 2–5 clusters have measurable transmission. Thus, by varying the delay from very early to very late extraction, where at the extreme delays no ions are detected anymore, we ensure that we account reliably for the total ion population in the trap by summing up all spectra (Fig. 1). To validate this approach further, mass spectra of $CH_3^+He_n$ are presented in Fig. 2 to allow for direct comparison with corresponding spectra recorded previously by Asvany and coworkers using a QPMS for ion analysis.[42] Attachment of only two He atoms is observed with significant abundance in both approaches, and the n = 3 abundance in the QPMS study is lower by three orders of magnitude than those of n = 1 and 2. The spectrum in Fig. 2 is taken at relatively long delay to illustrate the sharp drop in ion population at n = 2 also using the ReTOF approach, indicating shell closure at this cluster size. This observation is in line with the previous potential energy surface calculations for $CH_3^+He_n$ with n = 1–2,[15,26,27] and results from rotationally-resolved IRPD and microwave spectra.[26,42,77] These studies show that the first two He atoms strongly bind to the vacant and thus very electrophilic $2p_z$ orbital of C (D_e = 700 cm^{-1} for n = 1 at MP2/aug-cc-pVTZ), while binding to the protons is much less stable (D_e = 100 cm^{-1}),[26] so that $CH_3^+He_n$ with $n \geq 3$ are very difficult to grow even in cryogenic traps.[42] This view is fully supported by additional extensive IRPD studies and calculations of $CH_3^+Rg_n$ clusters with the larger rare gas atoms Ar ($n \leq 8$) and Ne ($n \leq 2$).[15,78,79] While in the supersonic plasma expansion only $CH_3^+He_n$ clusters with n = 1 could be produced in sufficient abundance for spectroscopy,[26] in the ion trap the n = 1 and 2 clusters are readily produced with enough abundance for spectroscopic interrogation.[77]

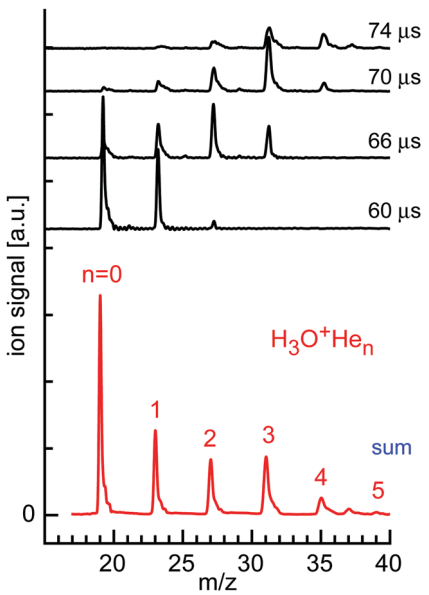

Fig. 1 Mass spectra of the ion trap content recorded with the ReTOF, when storing mass-selected H_3O^+ ions in the 22-pole trap and growing $H_3O^+He_n$ clusters. Individual mass spectra for variable delay times between ion extraction from the trap and ion extraction into the orthogonal ReTOF illustrate the transmission efficiency as a function of the delay. The sum spectrum is the sum of all spectra for delays between 50 and 84 μs in steps of 2 μs. In addition to the predominant $H_3O^+He_n$ series, $H_3O^+H_2O$ ($H_5O_2^+$) is observed at m/z 37.

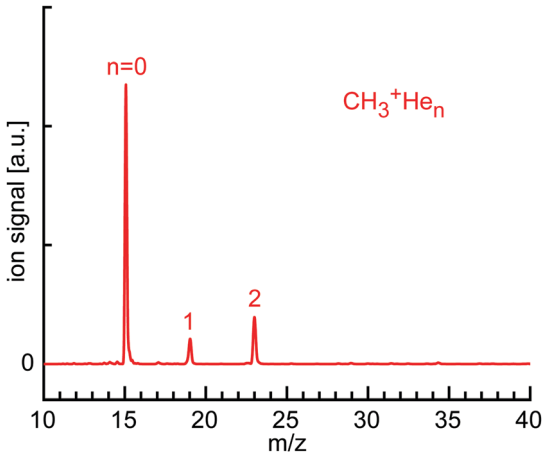

Fig. 2 Mass spectrum of the ion trap content recorded with the ReTOF, when storing mass-selected CH_3^+ ions in the 22-pole trap and growing $CH_3^+He_n$ clusters. This mass spectrum is taken at a long delay to illustrate the shell closure at n = 2.

Ab initio calculations at the unrestricted CCSD/aug-cc-pVTZ level with tight optimization are carried out for $H_2O^+He_n$, $H_3O^+He_n$, and $CH_3OH_2^+He_n$ clusters to determine their structure, binding energy, rotational constants, and vibrational frequencies.[80] Single point calculations are carried out at CCSD(T) level at the minima obtained at the CCSD level. Harmonic vibrational frequencies are scaled to optimize the agreement between computed and experimental OH stretch and bend frequencies of H_2O^+ and H_3O^+. Spin contamination is negligible, with values of $\langle S^2 \rangle - 0.75 < 10^{-2}$ (10^{-4}) before (after) spin annihilation for H_2O^+ and its clusters in the $^2A_1$ doublet ground state. As expected, popular DFT methods are not suitable to describe the interactions in this type of clusters. For example, our B3LYP-D3/aug-cc-pVTZ results for He_2 and H_2O^+He show that this level severely underestimates the He···He interaction (D_e = 0.2 cm^{-1}, R_e = 2.805 Å) and strongly overestimates the H_2O^+He interaction (D_e = 708.8 cm^{-1}, R_e = 1.591 Å) compared to results at the CCSD(T)/aug-cc-pVTZ level (D_e = 6.9 and

 This journal is © the Owner Societies 2022

Open Access Article. Published on 20 April 2022. Downloaded on 12/31/2025 2:24:13 PM.
This article is licensed under a Creative Commons Attribution 3.0 Unported Licence.

487.9 cm^{-1}, R_e = 3.015 and 1.702 Å). The latter values compare favorably with the best estimate for He_2 from Virial and viscosity data (D_e = 7.6 cm^{-1}, R_e = 2.963 Å)[81] and the CCSD(T)/CBS value for H_2O^+He (D_e = 482.0 cm^{-1}). The CCSD(T)/CBS values are obtained by extrapolation of the calculations with the aug-cc-pV*n*Z basis sets with n = 3–5 at the geometry of n = 3. We do not systematically include corrections for basis set superposition error (BSSE). For the global minimum of H_2O^+He, the CCSD(T)/aug-cc-pVTZ level yields D_e = 510.2 and 455.2 cm^{-1} without and with BSSE correction, respectively, while the CCDT(T)/CBS value amounts to 482.0 cm^{-1}. Hence, the BSSE correction lowers D_e by roughly 11%, while the limited basis set overestimates it by around 6%. In addition to equilibrium geometries and dissociation energies, we also evaluate binding energies (D_0) by considering harmonic zero-point vibrational corrections. We are aware that zero-point motions involve large-amplitude motions even in the ground vibrational state,[23,27] and these may not be well described by the harmonic approximation. To this end, the equilibrium energies D_e at the CCSD(T) level are more reliable. The atomic charge distribution is evaluated using the natural bond orbital (NBO) analysis.

3. Results and discussion

3.1 $H_2O^+He_n$

Fig. 3 shows the mass spectrum obtained for the growth of $H_2O^+He_n$ clusters around the mass-selected H_2O^+ ion. In addition to the very intense H_2O^+ parent ion (n = 0), $H_2O^+He_n$ clusters are produced with a higher intensity for n = 1, while signals for n = 2–4 are similar and around a factor of 3–5 weaker than for n = 1. The signal for n = 5 drops again by a factor of five, and the n = 6–9 peaks are barely visible. Clusters with $n \geq 10$ are below the detection limit. The relative signal intensities are 150 : 25 : 8 : 7 : 5 : 1 for n = 0–5, and $<$0.1 for n = 6–9. This mass spectrum

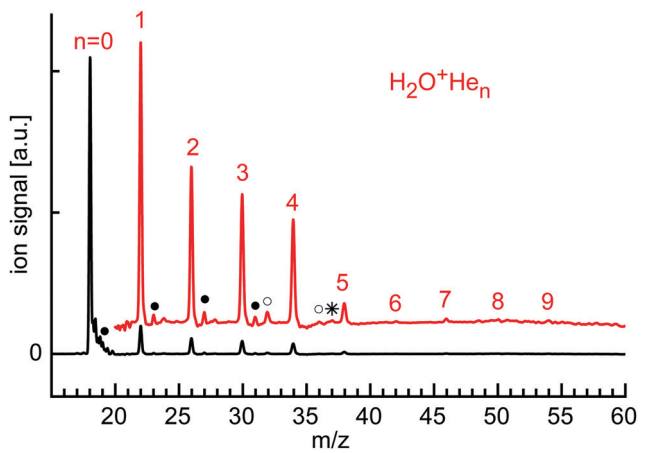

Fig. 3 Sum mass spectrum of the ion trap content recorded with the ReTOF, when storing mass-selected H_2O^+ ions in the 22-pole trap and growing $H_2O^+He_n$ clusters. The filled circles and the asterisk indicate the formation of $H_3O^+He_n$ (*m*/*z* 23, 27, 31) and $H_3O^+H_2O$ ($H_5O_2^+$, *m*/*z* 37), while the open circles are due $O_2^+He_{n\leq1}$ (*m*/*z* 32, 36), which are produced by O_2 impurity in the He line and exothermic charge transfer from H_2O to O_2.

suggests relatively stable and comparable binding sites for n = 1–4, while n = 5 seems less stable. After filling the solvation subshells with five He ligands, attachment of a sixth He atom seems not efficient due to even lower binding energy, and all efforts to change the experimental conditions for the He pulse (timing, intensity, duration) failed in producing $H_2O^+He_n$ clusters with $n \geq 10$. In addition to the main $H_2O^+He_n$ series, we detect also $H_3O^+He_{n\leq3}$ (*m*/*z* 23, 27, 31) and $H_3O^+H_2O$ (*m*/*z* 37), because the QPMS does not completely filter out all H_3O^+ ions produced in the EI source. We also detect $O_2^+He_{n\leq1}$ clusters (*m*/*z* 32, 36), which are produced by O_2 impurity in the He line and exothermic charge transfer from H_2O^+ to O_2.

In an effort to assign the observed $H_2O^+He_n$ cluster structures, we consider again the CCSD calculations, and the most stable isomers are shown in Fig. 4. Ionization of H_2O ($^1A_1$, C_{2v}) into its cation ground state ($^2B_1$, C_{2v}) occurs by removal of an electron from the nonbonding b_1 orbital, which is essentially the $2p_z$ orbital of O and thus perpendicular to the molecular plane. The structural data for H_2O^+ (r_e = 1.0001 Å, θ_e = 109.3°) and rotational constants (A_e = 28.119, B_e = 12.572, C_e = 8.688 cm^{-1}) are in excellent agreement with the experimental values (r_e = 0.9992(6) Å, θ_e = 109.3(1)°, A_e = 27.789, B_e = 12.588, C_e = 8.700 cm^{-1}).[82] The scaled harmonic vibrational frequencies of the symmetric and antisymmetric OH stretch modes of ν_1 = 3211 and ν_3 = 3261 cm^{-1} are also close to the measured fundamentals, ν_1 = 3213 and ν_3 = 3259 cm^{-1}.[82]

The potential energy surface of H_2O^+Rg dimers with Rg = He–Ar has been characterized in detail before by calculations at the MP2 and CCSD(T) levels.[24,83–89] It contains two nonequivalent minima, in which the Rg atom binds either to one of the protons forming a nearly linear OH···Rg ionic H-bond (two equivalent minima) or to the $2p_z$ orbital of O (also two equivalent minima), while other parts of the potential are less attractive. The H-bonded minima are stabilized by dispersion and induction forces (charge-induced dipole), while the p-bonded minima are stabilized by charge transfer from Rg into the $2p_z$ singly occupied orbital (SOMO). The latter is weak for small Rg atoms but becomes more pronounced for larger Rg atoms, because the ionization potential of Rg gets closer to that of H_2O (IP = 24.6, 21.6, 15.8, 14.0, 12.1 eV for He–Xe and 12.6 eV for H_2O),[90] Thus, for Rg = He–Ar the H-bonded isomer is the global minimum on the H_2O^+Rg potential and the p-bonded structure is clearly a higher lying local minimum, in agreement with the experimental IRPD spectra.[24,83,84,87] On the other hand, for Rg = Kr the hemi-bonded p-isomer is slightly more stable than the H-bonded isomer.[91,92]

For H_2O^+He, the CCSD calculations predict for $H_2O^+He(H)$ a planar structure (C_s) with a nearly linear OH···He bond, with intermolecular bond parameters (R_e = 1.702 Å, β_e = 174.2°, A_e = 21.539 cm^{-1}, B_e = 0.68900 cm^{-1}, C_e = 0.66765 cm^{-1}, D_e = 488 cm^{-1}, D_0 = 207 cm^{-1}), which are in good agreement with previous computational data[24,86] and experimental values from IRPD spectroscopy (R_0 = 1.656(4) Å, β_0 = 175(5)°, (B_0 + C_0)/2 = 0.6535 cm^{-1}).[24] The proton donor O–H bond considerably elongates (by 2.3 mÅ) upon H-bonding, while the free O–H bond slightly contracts (by 1.0 mÅ). As a result, the ν_1

Open Access Article. Published on 20 April 2022. Downloaded on 12/31/2025 2:24:13 PM.
This article is licensed under a Creative Commons Attribution 3.0 Unported Licence.

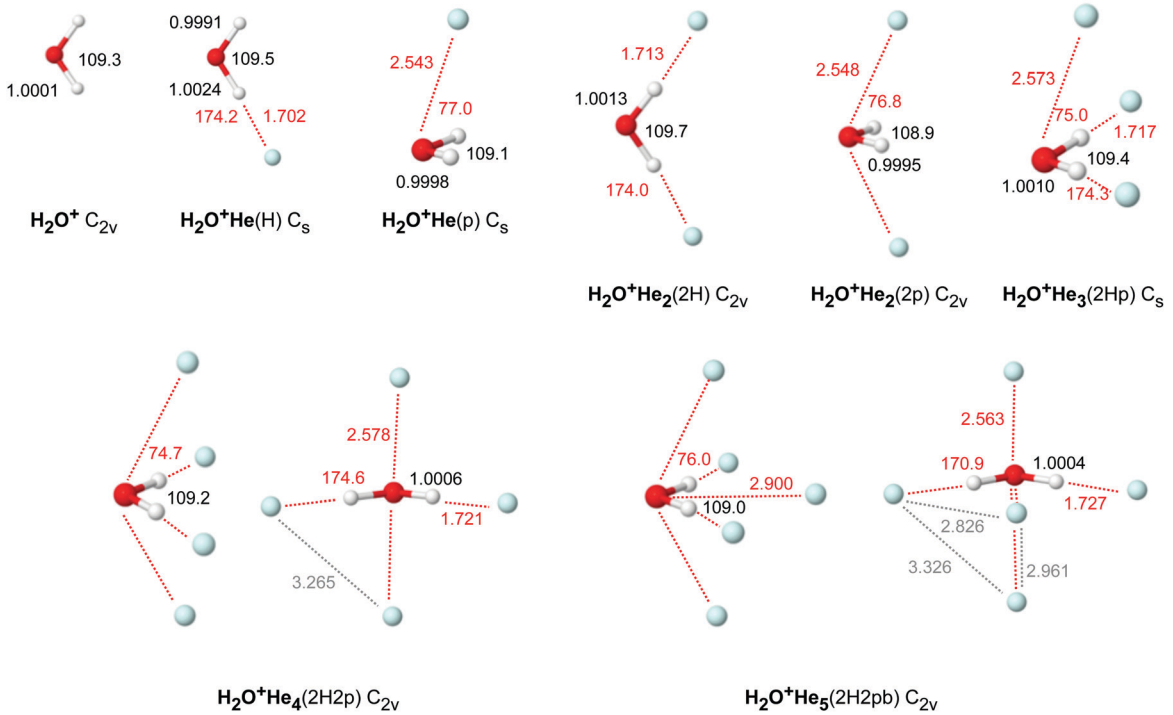

Fig. 4 Minimum structures (in Å and degree) of $H_2O^+He_n$ with n = 0–6 obtained at the CCSD/aug-cc-pVTZ level.

and ν_3 frequencies display both red shifts of −27 and −8 cm^{-1}, in qualitative agreement with the observed values (−15 and −5 cm^{-1}).[24] The weak interaction of H_2O^+ with He is insufficient to decouple ν_1 and ν_3 into the two equivalent OH stretch local modes, leading to a red shift in ν_3 (mostly free OH stretch) although the free O–H bond contracts upon forming the OH···He H-bond. In fact, the barrier between the two equivalent H-bonded minima at a planar transition state is rather low so that tunneling splittings for hindered internal rotation could be resolved in the IRPD spectra of H_2O^+He, which are absent in the HDO^+He spectra. This tunneling motion, along with the involved large amplitude motion, also explains the overestimation of the computed $\Delta\nu_{1/3}$ shifts calculated for the rigid $H_2O^+He(H)$ equilibrium structure because the He moves away from the linear OH···He configuration even for the zero-point level. H-bond formation slightly increases the H_2O bend angle by 0.2°. It also increases the H_2O^+ bend frequency by $\Delta\nu_2$ = +4 cm^{-1}, due to the additional retarding force of the OH···He bond.

The CCSD calculations predict for the local $H_2O^+He(p)$ minimum (C_s) a structure, in which the He is attached to H_2O in the plane perpendicular to the molecular plane. The He ligand is slightly tilted away from the $2p_z$ orbital toward the OH protons. The predicted intermolecular bond parameters for the O···He bond are R_e = 2.543 Å, β_e = 77.0°, A_e = 9.0835 cm^{-1}, B_e = 0.78853 cm^{-1}, C_e = 0.75945 cm^{-1}, D_e = 270 cm^{-1}, and D_0 = 99 cm^{-1}. The O–H bonds slightly contract upon He attachment at the $2p_z$ orbital (by 0.3 mÅ) and, as a result, the computed ν_1 and ν_3 frequencies display both minor blue shifts of 4 cm^{-1}. This effect is mostly caused by the small electron transfer from He into the electrophilic $2p_z$ SOMO orbital of H_2O^+, which makes the cation slightly less positively charged and thus shifts the low-frequency $\nu_{1/3}$ modes of H_2O^+ toward the higher-frequency modes of neutral H_2O. Such blue-shifted vibrational transitions are absent in the IRPD spectrum, clearly confirming that the H-bonded isomer is the global minimum on the H_2O^+He potential.[24] In contrast to the H-bonded isomer, p-bonding decreases the H_2O bond angle by 0.2° but also increases ν_2 by 3 cm^{-1}. Overall, the CCSD results for $H_2O^+He(p)$ are close to those reported earlier at the MP2 level.[24,86]

In the planar global minimum structure of $H_2O^+He_2(2H)$ with C_{2v} symmetry, two equivalent OH···He H-bonds are formed, which are only slightly weaker than that in the $H_2O^+He(H)$ dimer, with R_e = 1.713 Å, β_e = 174.0°, D_e = 472 cm^{-1}, and D_0 = 228 cm^{-1}. In principle, the two He atoms do not interact much with each other and one expects near additivity in the properties and effects upon sequential He solvation. The observation of slightly less than additivity is consistent with the noncooperative threebody forces of interior ion solvation. This effect arises from nonadditive induction forces and charge delocalization, which are both small due to the weak interaction. Both proton donor O–H bonds considerably elongate (by 1.2 mÅ) upon H-bonding, causing total red shifts of −21 and −41 cm^{-1} in ν_1 and ν_3. H-bond formation slightly increases the H_2O bend angle by 0.4° and ν_2 by +7 cm^{-1} compared to bare H_2O^+, again nearly twice the changes caused by the first OH···He bond.

For comparison, we have also computed the $H_2O^+He_2(2p)$ local minimum with C_{2v} symmetry. As expected, it has two equivalent O···He p-bonds, which are only slightly weaker than that in the $H_2O^+He(p)$ dimer due to slightly noncooperative threebody forces (R_e = 2.548 Å, β_e = 76.8°, D_e = 266 cm^{-1},

 This journal is © the Owner Societies 2022

Open Access Article. Published on 20 April 2022. Downloaded on 12/31/2025 2:24:13 PM.
This article is licensed under a Creative Commons Attribution 3.0 Unported Licence.

D_0 = 139 cm^{-1}). The free O–H bonds contract by 0.6 mÅ, resulting in total blue shifts of 9 cm^{-1} in both ν_1 and ν_3 from the values of bare H_2O^+. The H_2O bond angle increases by 0.4° and ν_2 increases by 5 cm^{-1}.

The most stable n = 3 and n = 4 clusters are obtained by adding two p-bonded He ligands to $H_2O^+He_2$(2H), resulting in $H_2O^+He_3$(2Hp) and $H_2O^+He_4$(2H2p) with C_s and C_{2v} symmetry. The p-bonds in n = 3 and 4 are slightly longer (R_e = 2.573 and 2.578 Å) and weaker (D_e = 264 and 261 cm^{-1}, D_0 = 160 and 158 cm^{-1}) than in the p-bonded isomers of n = 1 and 2. Again, p-bonding slightly contracts the O–H bonds compared to $H_2O^+He_2$(2H) by 0.3 and 0.6 mÅ, causing blue shifts in both ν_1 and ν_3 of 5/10 cm^{-1} for n = 3/4. The H_2O bond angle decreases by 0.2° and ν_2 increases by 3 cm^{-1} for each p-bonded ligand. Moreover, p-bonding destabilizes the OH···He bonds, which elongates by 4 mÅ for each p-bonded ligand. This trend is in line with strengthening the intramolecular O–H bonds, which reduces their acidity and thus their propensity to form H-bonds.

After all four minima on the H_2O^+He dimer potential are filled with two H-bonded and two p-bonded He ligands, the fifth ligand occupies a less stable binding site, which is not a minimum on the dimer potential. Inspection of the in-plane and out-of-plane potential characterized by MP2 suggests that the O end is not very favorable because of the repulsive in-plane lone pair of O.[24] On the other hand, the proton side is rather attractive. Hence, a natural attractive binding site is in the H_2O^+ plane on the C_2 axis between the two H-bonded He ligands, leading to a $H_2O^+He_5$ structure with C_{2v} symmetry and binding energies (D_e = 251 and D_0 = 161 cm^{-1}) not much lower than those of the p-bonded ligands. Indeed, the p-bonded minimum on the MP2 dimer potential is very shallow and has a low barrier for migration toward the position of the fifth He ligand.[24] At this bridged position, it has a distance of 2.900 Å from O, 2.458 Å from the two protons, and 2.827 and 2.961 Å from the H-bonded and p-bonded He atoms. The latter distances are close to the He–He distance in He_2 of 2.805 Å, consistent with close packing. Attachment of the fifth ligand weakens and thus lengthens the OH···He H-bonds (by 6 mÅ), while the O···He p-bonds become slightly shorter (by 16 mÅ). As a result of the weaker H-bonds and the stronger p-bonds, the O–H bonds become shorter (by 0.2 mÅ), resulting in blue shifts of ν_1 and ν_3 by +4 and +3 cm^{-1}. The H_2O bend angle becomes smaller (by 0.2°) and ν_2 decreases by 3 cm^{-1}.

The $H_2O^+He_n$ cluster growth deduced from the CCSD calculations suggests the initial formation of the in-plane H-bonded minima with binding energies of $D_e \sim$ 480 cm^{-1}, followed by out-of-plane p-bonded He-ligands with much weaker binding of $D_e \sim$ 260 cm^{-1} and the bridged ligand with similar interaction ($D_e \sim$ 250 cm^{-1}) (Fig. 5 and Table 1). At n = 5, all favorable binding sites are occupied by He atoms, as suggested by the H_2O^+He dimer potential, which suggests for the O binding site only weak He binding ($D_e \sim$ 60 cm^{-1}) due to repulsion from the lone pair.[24] Apparently, the mass spectrum in Fig. 3 is fully consistent with this view, showing only minor abundances for $H_2O^+He_n$ clusters with $n \geq 6$. Interestingly, the intensity of n = 5

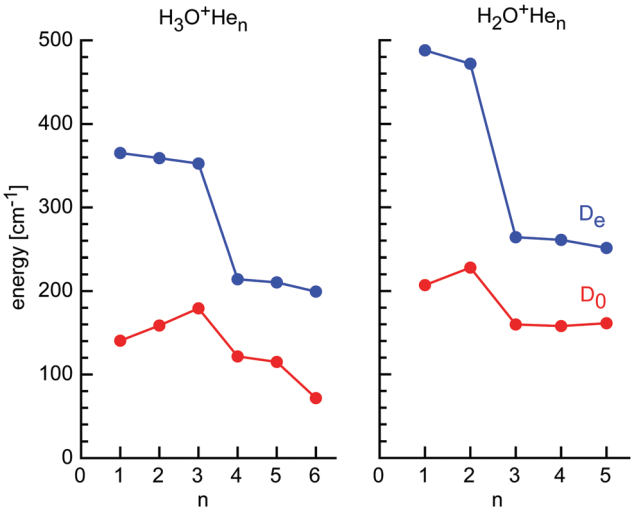

Fig. 5 Incremental He binding energies (D_e and D_0) of $H_3O^+He_n$ and $H_2O^+He_n$ clusters calculated at the CCSD/aug-cc-pVTZ level.

Table 1 Binding energies of the He atoms in $H_2O^+He_n$ and $H_3O^+He_n$ evaluated at the CCSD/aug-cc-pVTZ level (in cm^{-1})[a]

	H_2O^+		H_3O^+		$CH_3OH_2^+$	
n	D_e	D_0	D_e	D_0	D_e	D_0
1 (H)	487.9 (510.2)	207.0	365.2 (384.9)	139.9	283.6 (301.7)	140.0
1 (p)	269.7 (282.1)	99.4				
2 (2H)	471.8 (492.5)	228.0	359.1 (378.1)	158.7	281.8 (299.4)	140.1
2 (2p)	266.0 (278.1)	138.7				
3	264.1 (276.2)	159.8	352.6 (371.1)	179.3		
4	260.9 (259.0)	157.9	214.2 (225.9)	121.6		
5	251.2 (277.5)	161.3	210.4 (221.4)	115.0		
6			199.4 (212.9)	71.6		

[a] Numbers in parentheses are CCSD(T) energies (single-point calculations at the CCSD geometry).

is substantially reduced compared to n = 3–4, although these cluster sizes have similar He binding energies. This result may indicate the quantum nature of the He motion. While in $H_2O^+He_n$ with n = 1–4 the He ligands can readily undergo large amplitude motions, the structure of the n = 5 cluster is rather compact and more rigid due to close-packing of all five ligands, thereby strongly reducing the possibility for large amplitude motions even at 0 K, whereby this effect is larger for the angular than the stretching motions. As a result, even though the interaction energy for the fifth He atom is quite favorable, the large zero-point motions may make it difficult for the He ligand to squeeze into this binding site, thereby reducing its effective binding energy and population. The cluster growth deduced herein from mass spectrometry and CCSD calculations is fully consistent with the one derived for $H_2O^+Ar_n$ clusters derived from IRPD spectroscopy (n = 1–14) and MP2 calculations (n = 1–4).[84,88,93] As expected, the charge transfer from H_2O^+ to the individual He ligands is small, and the NBO charges per He atom are 9, 1, and 0.3 me for the H-bonded, p-bonded, and bridged ligands, and decrease slightly as the cluster grows (Table S1 in ESI†).

Open Access Article. Published on 20 April 2022. Downloaded on 12/31/2025 2:24:13 PM.
This article is licensed under a Creative Commons Attribution 3.0 Unported Licence.

Significantly, while the H_2O^+He dimer has been produced in a supersonic plasma expansion and spectroscopically characterized by IRPD previously, the larger $H_2O^+He_n$ clusters with n = 2–9 are generated herein for the first time. Similar to the $CH_3^+He_n$ case, this result demonstrates the superior performance of ion traps over supersonic expansions in growing larger X^+He_n clusters. This is in contrast to $H_2O^+Rg_n$ with the larger Rg atoms Ar and Kr, which have been grown and studied up to n = 14 and 3, respectively.[93,94] Fig. 6 summarizes the predicted evolution of the OH stretch and H_2O bend frequencies ν_{1-3} as a function of cluster size for the size range n = 0–5 as basis for future IRPD spectroscopy and includes the available experimental data for n = 0 and 1 (Table S2 in ESI†). As can be seen, the H-bonded ligands cause large incremental red shifts in ν_1 and ν_3 due to destabilization of the O–H bonds by the formation of OH···He H-bonds (~15 cm^{-1} on average) and smaller blue shifts of 4 cm^{-1} in ν_2 due to the additional retarding force of the H-bonds. On the other hand, p-bonded ligands cause only minor blue shifts in ν_1 and ν_3 (~5 cm^{-1}) due to modest charge transfer into the $2p_z$ orbital of O which strengthens the O–H bonds and similarly small blue shifts in ν_2 (~3 cm^{-1}). Interestingly, the bridged He ligand (n = 5) causes a similarly small blue shift in ν_1 and ν_3 as the p-bonded ligand but a red shift in ν_2. Hence, the pattern in the ν_{1-3} frequencies will readily allow for distinguishing the various isomeric structures. In addition to the frequency pattern, the computed IR intensities are reported in Table S2 in ESI.† All fundamentals of H_2O^+ are strongly IR active. While H-bonded He ligands strongly increase the IR activity in ν_1 and ν_3 and slightly reduce that of ν_2, p-bonded ligands have little impact on the intensity of all three modes. Overall, the spectral pattern predicted for $H_2O^+He_n$ is similar to that predicted and observed for $H_2O^+Ne_n$ and $H_2O^+Ar_n$, whereby the effects scale with the polarizability of the Rg atom. A detailed comparison of the H_2O^+Rg dimer potentials, structures, energies, and spectral shifts has been presented elsewhere.[24]

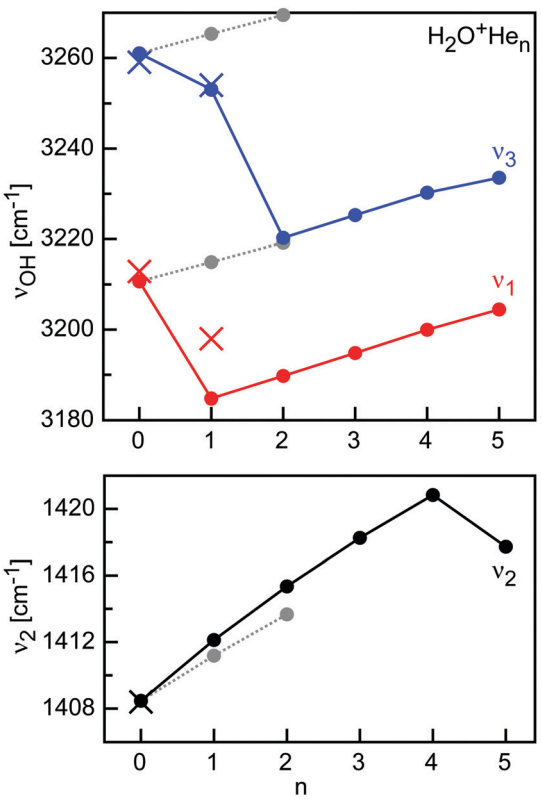

Fig. 6 OH stretch (ν_1 and ν_3, scaled by 0.9442) and O–H bend (ν_2, scaled by 0.9492) frequencies calculated for $H_2O^+He_n$ clusters (CCSD/aug-cc-pVTZ) compared to available experimental values for n = 0 and 1 (crosses).

3.2 $H_3O^+He_n$

Fig. 1 shows the mass spectrum obtained for the growth of $H_3O^+He_n$ clusters around the mass-selected H_3O^+ ion. In addition to the very intense H_3O^+ parent ion (n = 0), $H_3O^+He_n$ clusters are produced with a higher intensity for n = 1–3, while signals drop for n = 4–5 and disappear for n = 6. The relative signal intensities are roughly 125 : 50 : 30 : 30 : 10 : 1 for n = 0–5. This mass spectrum suggests relatively stable and comparable binding sites for n = 1–3 by forming OH···He ionic H-bonds to the three available OH protons. After filling this solvation subshell with three He ligands, further attachment occurs at less stable binding sites. In addition to the $H_3O^+He_n$ series, we detect again $H_3O^+H_2O$ (m/z 37) from H_2O impurity in the He line or residual gas pressure in the trap. The observed mass spectrum is similar to that obtained recently in a cryogenic trap coupled to a QPMS, again validating our approach.[34] Actually, the latter study observed the n = 6 cluster about a factor 10 weaker than the n = 5 cluster.

To rationalize the observed $H_3O^+He_n$ cluster growth, we consider again the CCSD calculations and the most stable isomers are shown in Fig. 7. Protonation of H_2O produces the pyramidal H_3O^+ cation with C_{3v} symmetry and a low barrier for inversion through the planar D_{3h} transition state. The equilibrium structural data for H_3O^+ (r_e = 0.9769 Å, θ_e = 111.7°) and rotational constants (B_e = 11.028, C_e = 6.4006 cm^{-1}) are in excellent agreement with the experimental values (r_e = 0.974(1) Å, θ_e = 113.6(1)°, B_e = 11.2329(26), C_e = 6.2913(66) cm^{-1}).[95] The scaled harmonic vibrational frequencies of the symmetric and degenerate antisymmetric OH stretch modes of ν_1(a) = 3439 and ν_3(e) = 3529 cm^{-1} are also close to the measured fundamentals, ν_1 = 3440 and ν_3 = 3528 cm^{-1} (average of tunneling components).[95,96]

The global minima for the $H_3O^+He_n$ clusters with n = 1–3 are characterized by n equivalent and nearly linear OH···He ionic H-bonds, leading to structures with C_s, C_s, and C_{3v} symmetry. Due to small noncooperative threebody forces, the strength of the H-bonds decreases roughly linearly with n, as indicated by the intermolecular bond lengths of R_e = 1.800, 1.808, and 1.816 Å, and the equilibrium binding energies, D_e = 365, 359, and 353 cm^{-1} (Table 1), respectively. This trend is also visible in the charge transfer from H_3O^+ per He atom of 8.5, 8.1, and 7.9 me (Table S1 in ESI†). The zero-point corrected energy shows the opposite trend, D_0 = 140, 159, and 179 cm^{-1}, illustrating the subtle effect of the vibrations on the dissociation energy, although the harmonic correction may not be reliable for these floppy clusters. The OH···He bond angle

 This journal is © the Owner Societies 2022

Open Access Article. Published on 20 April 2022. Downloaded on 12/31/2025 2:24:13 PM.
This article is licensed under a Creative Commons Attribution 3.0 Unported Licence.

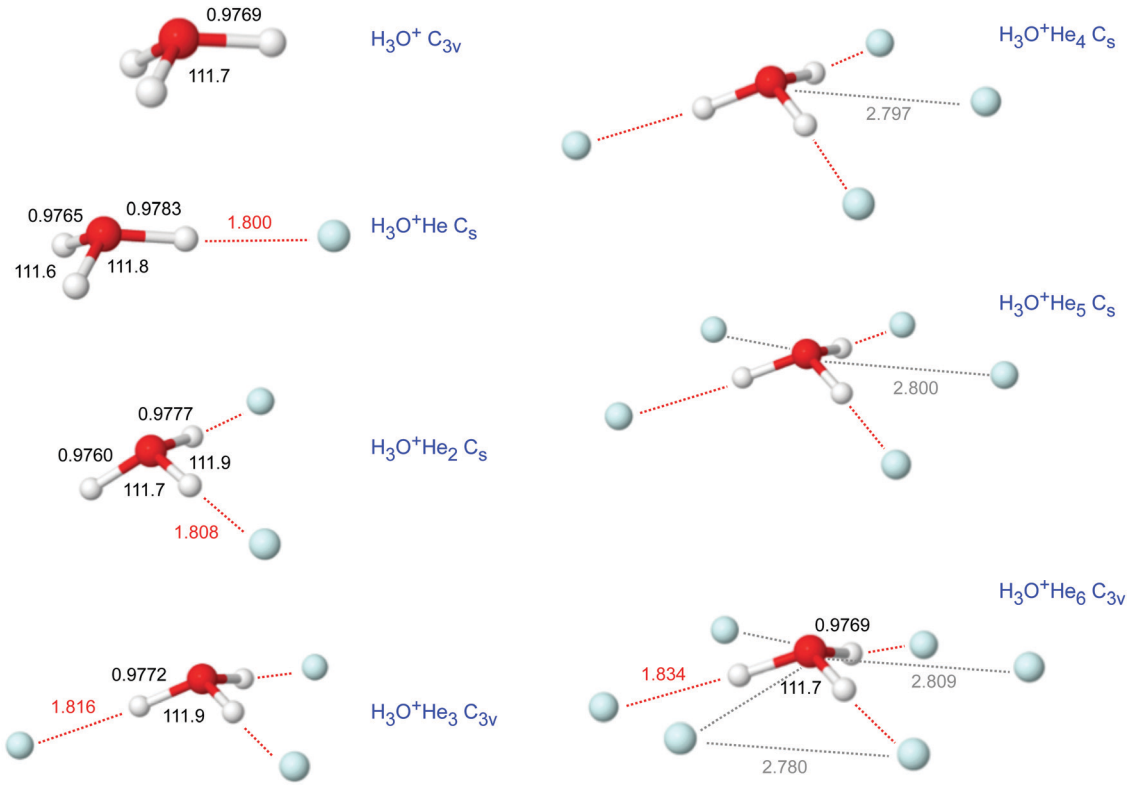

Fig. 7 Minimum structures (in Å and degree) of $H_3O^+He_n$ with n = 0–6 obtained at the CCSD/aug-cc-pVTZ level.

changes from 175.0 to 174.8° for n = 1 and 3, respectively, while the H_3O^+ ion gets more planar (θ_e = 111.7 and 111.9° for n = 0 and 3). The bound O–H bonds elongate upon H-bonding (by 1.4, 0.8, and 0.3 mÅ for n = 1–3), while the free O–H bonds contract (by 0.4 and 0.9 mÅ for n = 1–2). Overall, the properties derived here for H_3O^+He are consistent with previous CCSD calculations of the dimer potential.[97,98]

In contrast to the open-shell H_2O^+ cation with its partly occupied and electrophilic $2p_z$ orbital, the closed-shell H_3O^+ cation has a filled and thus for He repulsive $2p_z$ orbital of the central O atom. As a result, this region of p-bonding to H_3O^+ is not favorable for He ligands. For example, the O-bound structure of H_3O^+He with C_{3v} symmetry is a transition state between the H-bound minima with a very low binding energy (D_e = 95 cm^{-1}, D_0 = 39 cm^{-1}, R_e = 3.049 Å). Hence, they prefer to occupy positions between the H-bonded He ligands, leading to structures with C_s, C_s, and C_{3v} symmetry for n = 4–6. The plane of the n = 4–6 ligands is only slightly above the plane of the n = 1–3 ligands, so that the He ligands in $H_3O^+He_6$ form a slightly distorted regular hexagon with He–He distances of 2.8 Å in close agreement with the van der Waals distance in He_2 (2.805 Å). The equilibrium binding energies in this second shell are much lower than in the first H-bonded shell, with D_e = 214, 210, and 199 cm^{-1} for n = 4–6, respectively, and this trend is also visible in the reduced charge transfer from H_3O^+ per He atom of 1.9 me. The slight decrease in D_e with size is again due to small noncooperativity and results in an increase in the O–He distance from 2.797 to 2.809 Å for n = 4–6. Interestingly, the dissociation energies show a significant drop for n = 4–6 (D_0 = 122, 115, and 72 cm^{-1}), and the drop is particularly large for the last ligand. Due to enhanced charge delocalization, the formation of the second He ring also weakens the bonds to the first H-bonded He ring, whose bond lengths elongate from 1.816 Å in n = 3 to 1.834 Å in n = 6. Formation of the second He shell makes the H_3O^+ ion again slightly less planar and the pyramidal angle in n = 6 is again the same as in n = 0 (111.7°).

The $H_3O^+He_n$ cluster growth deduced from the CCSD calculations is fully consistent with the mass spectrum shown in Fig. 1. The first solvation shell has three H-bonded H-ligands with similarly high binding energies, giving rise to similar intensities in the mass spectrum. The signals drop for the three bridged He atoms, which have substantially lower binding energies. Similar to the $H_2O^+He_n$ case, it appears not easy to squeeze in the last two ligands (n = 5 and n = 6), probably again by quenching the possibility for large-amplitude motion of the first ligands. This causes higher intermolecular frequencies and thus larger zero-point energy, which reduces the binding energies, as seen for the low D_0 value computed for n = 6. The deduced cluster growth is fully consistent with the H_3O^+He dimer potential,[97,98] and the computational and spectroscopic studies of $H_3O^+L_n$ clusters with larger Rg atoms and small inert ligands (L = N_2, CO_2).[99–104]

While the vibrational spectroscopy of H_3O^+ is known for long time by high-resolution spectroscopy, no spectral data appear to be available for its $H_3O^+He_n$ clusters. In the C_{3v}

Open Access Article. Published on 20 April 2022. Downloaded on 12/31/2025 2:24:13 PM.
This article is licensed under a Creative Commons Attribution 3.0 Unported Licence.

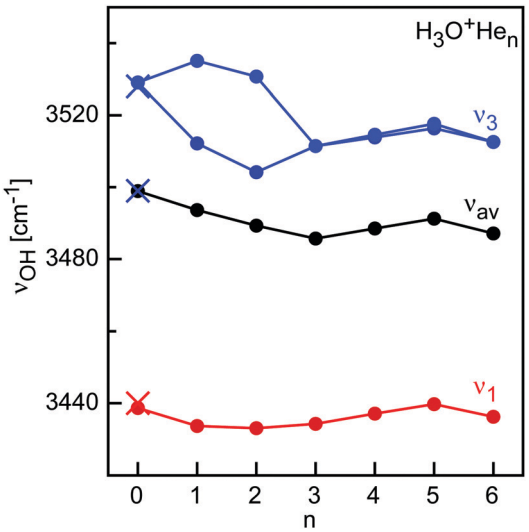

Fig. 8 OH stretch (ν_1 and ν_3) frequencies calculated for $H_3O^+He_n$ clusters (CCSD/aug-cc-pVTZ, scaling factor 0.9505, filled circles) compared to available experimental values for n = 0 (crosses).

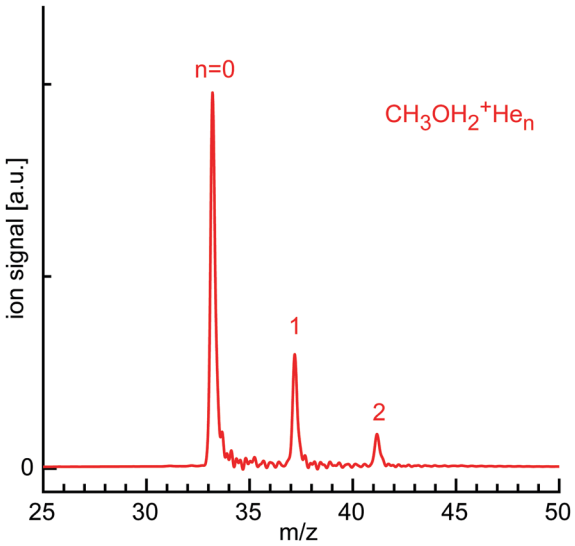

Fig. 9 Sum mass spectrum of the ion trap content recorded with the ReTOF, when storing mass-selected $CH_3OH_2^+$ ions in the 22-pole trap and growing $CH_3OH_2^+He_n$ clusters.

symmetric equilibrium structure, H_3O^+ has two OH stretch normal modes, namely the symmetric ν_1(a) and antisymmetric degenerate ν_3(e) mode, which are split by inversion tunneling. Herein, we do not consider this tunneling motion, which will be strongly affected by He solvation, and thus focus on the average frequencies of the two tunneling components, measured as ν_1 = 3440 and ν_3 = 3528 cm^{-1}.[95,96] Complexation with n = 1, 2, 4, and 5 He atoms reduces the three-fold symmetry and thus removes the degeneracy of ν_3. The predicted evolution of the ν_1 and ν_3 components of $H_3O^+He_n$ as a function of n is illustrated in Fig. 8 (Table S3 in ESI†), along with the average OH stretch frequency (ν_{av}). The spectral shifts and splittings are larger for the H-bonded He ligands due to the stronger interaction, and an overall red shift of 13 cm^{-1} per atom is obtained. On the other hand, the bridged He atoms cause incremental blue shifts of 3 cm^{-1} for n = 4 and 5, while shell closure at n = 6 causes a small red shift (4 cm^{-1}). $H_3O^+L_n$ clusters with larger Rg ligands and small ligands show a similar pattern as a function of cluster size but with larger shifts and splittings due to the stronger $H_3O^+\cdots$L interaction.[99–104]

3.3 $CH_3OH_2^+He_n$

Fig. 9 shows the mass spectrum obtained for the growth of $CH_3OH_2^+He_n$ clusters around the mass-selected $CH_3OH_2^+$ ion, which is in good agreement with a recent report.[43] In addition to the prominent $CH_3OH_2^+$ parent peak (n = 0), only $CH_3OH_2^+He_n$ clusters with n = 1–2 are produced with significant abundance (relative ratio of roughly 10 : 3 : 1 for n = 0–2). This mass spectrum suggests relatively stable and comparable binding sites for n = 1–2 by forming OH$\cdots$He ionic H-bonds to the two available OH protons. In contrast to the related H_3O^+ ion, no further He atoms can be attached under our experimental conditions, because the CH_3 group is not attractive for He. In addition, the overall $ROH_2^+\cdots$He interaction becomes weaker upon H → CH_3 substitution due to enhanced charge delocalization. As a result, the OH protons in $CH_3OH_2^+$ are less acidic than in H_3O^+ leading to weaker OH$\cdots$He bonds. Moreover, the binding energy for the bridged binding site becomes too weak in $CH_3OH_2^+He_3$ and thus is not observed. To rationalize the observed cluster growth and the qualitative conclusions, we consider again the CCSD calculations.

Our CCSD optimization for $CH_3OH_2^+$ yields a pyramidal structure, which agrees well with previous calculations at a similar level (Fig. 10).[43] The O–H bonds are slightly shorter than in H_3O^+ (by 4 mÅ), leading to symmetric and antisymmetric OH stretch frequencies of $\nu_{OH}^{s/a}$ = 3510 and 3585 cm^{-1}, which are substantially higher than for H_3O^+ using the same scaling factor (3439 and 3529 cm^{-1}, Table S4 in ESI†). The oxonium ion is less pyramidal in $CH_3OH_2^+$, although the HOH

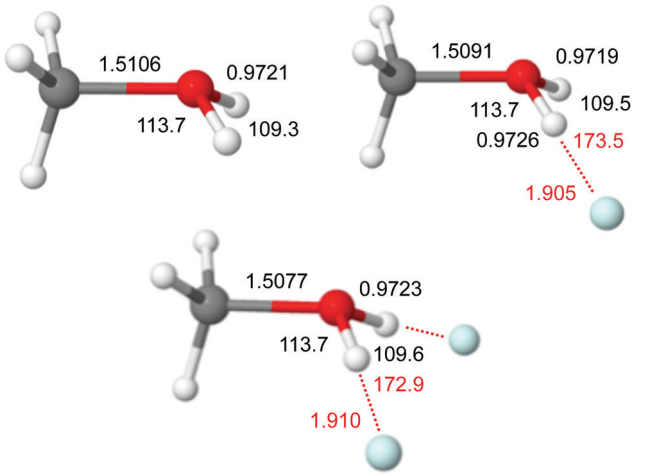

Fig. 10 Minimum structures (in Å and degree) of $CH_3OH_2^+He_n$ with n = 0–2 obtained at the CCSD/aug-cc-pVTZ level.

This journal is © the Owner Societies 2022

Open Access Article. Published on 20 April 2022. Downloaded on 12/31/2025 2:24:13 PM.
This article is licensed under a Creative Commons Attribution 3.0 Unported Licence.

bond angle is substantially smaller, β_e = 109.3 *vs.* 111.7°. So far, no IR spectrum of cold and isolated $CH_3OH_2^+$ has been reported, preventing any direct comparison to experiment. An IRPD spectrum of warm $CH_3OH_2^+$ produced by CO_2 elimination of protonated methyl formate shows only a single broad band centered at 3450 cm^{-1} (width 300 cm^{-1}), which is substantially red shifted from the spectrum predicted for cold $CH_3OH_2^+$ due to high internal temperature.[105]

The only previous experimental and computational study for $CH_3OH_2^+He_n$ reports only B3LYP calculations for n = 1, which strongly overestimates the interaction energy. Our CCSD data yield nearly linear intermolecular OH···He bonds with R_e = 1.905 and 1.910 Å, β_e = 109.5 and 109.6°, and D_e = 284 and 282 cm^{-1} for n = 1 and 2, respectively. The weaker OH···He bonds go along with smaller charge transfer from the cation to the He ligands (3 m*e* per He, Table S1 in ESI†). As the O–H bonds in $CH_3OH_2^+$ are stronger and less acidic than in H_3O^+, the intermolecular OH···He bonds are somewhat weaker in $CH_3OH_2^+He_n$. Consequently, the corresponding O–H bond elongations and red shifts in the OH stretch frequencies are smaller (Δr_{OH}^{av} = 1.5 and 0.5 mÅ, $\Delta\nu_{OH}^{s/a}$ = −1.7/−3.7 and −1.6/−7.8 cm^{-1} for n = 1 and 2). The computed frequencies for n = 1, $\nu_{OH}^{s/a}$ = 3508/3581 cm^{-1}, agree well with the measured ones, 3504/3571 cm^{-1}.[43] No spectral OH stretch data are available for n = 2. Interestingly, the C–O bond of $CH_3OH_2^+$ is also substantially affected by He complexation, with bond contractions of 1.5 mÅ per He atom and blue shifts in the CO stretch mode near 800 cm^{-1} of 5 cm^{-1}. In the limit of considering $CH_3OH_2^+$ as dative bond between CH_3^+ and OH_2, the strengthening of the C–O bond may be rationalized by a lowering of the ionization energy of the H_2O moiety, leading to a slightly stronger bond. Finally, we note that our CCSD structure of $CH_3OH_2^+He$ (R_e = 1.905 Å) is rather different from the B3LYP and B3LYP-D3 structures reported recently (R_e = 1.833 and 1.809 Å),[43] again due to the failure of these DFT methods to properly describe the X^+···He interaction (severe overestimation).

4. Conclusions

In summary, He cluster growth around the small cations X = H_2O^+, H_3O^+, and $CH_3OH_2^+$ in a cryogenic ion trap has been characterized by mass spectrometry and high level CCSD(T) calculations to determine the structural, vibrational, and energetic properties of X^+He_n clusters. The abundances of the cluster ions provide valuable experimental insight about the stepwise solvation process and the structure of the first solvation shell. Clearly, the cluster growth is fully controlled by the radial and angular properties of X^+···He dimer potential, because the He···He interaction is much weaker. In all cases, the cluster growth begins with the formation of equivalent OH···He ionic H-bonds leading to highly symmetric structures (first coordination), before less stable binding sites are occupied. In the case of the open-shell $H_2O^+He_n$ clusters, the latter are p-bonds to the partly filled electrophilic $2p_z$ orbital of O (second coordination). These binding sites are not favorable for $H_3O^+He_n$, because the filled $2p_z$ orbital is not attractive for the electron-avoiding He atoms. As a result, the second coordination shell has He atoms between the H-bonded He atoms, leading to a nearly planar and almost regular hexagon for n = 6. Overall, the strengths of the OH···He bonds scale with the proton affinity of the proton donor, which varies as PA = 593.2 < 691 < 754.3 kJ mol^{-1} for OH, H_2O, and CH_3OH.[106] The higher the PA, the stronger and less acidic the intermolecular O–H bonds (r_e = 0.9991, 0.9769, 0.9721 Å), the weaker the OH···He bonds (R_e = 1.702, 1.800, 1.905 Å; D_e = 488, 365, 284 cm^{-1}), and the smaller the charge transfer to He (q = 9, 5, 3 m*e*). As a consequence of the weaker OH···He bonds, their impact on the O–H bond elongation and reduction in the OH stretch frequencies are smaller, too. Overall, the binding energies for equivalent binding sites are almost the same, apart from a very minor noncooperative three-body effect, resulting mostly from nonadditive induction. Indeed, the dipole moments induced in the He atoms are not aligned favorably in the structures given by the strong X^+···He dimer two-body potential. Overall, the He atoms are arranged such that they have roughly the He···He van der Waals distance of ∼3 Å. The more He atoms are added to the solvation shell, the more rigid the cluster structure. As a result of restricted possibility for large-amplitude motions (in particular in the angular direction), the zero-point energy increases, which reduces the binding energy (D_0), and this leads to reduced population of equivalent binding sites as n increases. This effect may be probed in the future by advanced quantum calculations, including nuclear quantum effects, dynamics, and effects of temperature and the bosonic character of He. In general, the structured growth of the X^+He_n clusters is not only visible in their geometric and energetic properties but nicely reflected also in the evolution of the vibrational properties (both in frequency and IR intensity).

This work paves the way for several future directions. So far, from the clusters considered herein, only for the H_2O^+He dimer potential has been characterized in detail by high-resolution IRPD spectroscopy at the rotation–vibration-tunneling level. To this end, the larger $H_2O^+He_n$ clusters produced herein for the first time are further attractive targets for future IRPD experiments using the reliable CCSD predictions for these clusters. Similarly, no spectroscopic information is available yet for any of the $H_3O^+He_n$ clusters, and our presented CCSD predictions provide again a useful guide for such experiments. The open-shell $H_2O^+He_n$ clusters offer also the potential for optical spectroscopy as a probe for cluster structure.[107]

Conflicts of interest

There are no conflicts of interest to declare.

Acknowledgements

This study was supported by Deutsche Forschungsgemeinschaft (DFG, grant DO 729/8). We thank A. Günther, P. Nieto and D. Hauer-Vidal for support in the initial stage of this study.

Open Access Article. Published on 20 April 2022. Downloaded on 12/31/2025 2:24:13 PM.
This article is licensed under a Creative Commons Attribution 3.0 Unported Licence.

References

1 S. Grebenev, J. P. Toennies and F. Vilesov Andrei, *Science*, 1998, **279**, 2083–2086.
2 M. Hartmann, R. E. Miller, J. P. Toennies and A. Vilesov, *Phys. Rev. Lett.*, 1995, **75**, 1566–1569.
3 J. Tang, Y. Xu, A. R. W. McKellar and W. Jäger, *Science*, 2002, **297**, 2030–2033.
4 L. A. Surin, A. V. Potapov, B. S. Dumesh, S. Schlemmer, Y. Xu, P. L. Raston and W. Jäger, *Phys. Rev. Lett.*, 2008, **101**, 233401.
5 M. J. Weida, J. M. Sperhac, D. J. Nesbitt and J. M. Hutson, *J. Chem. Phys.*, 1994, **101**, 8351–8363.
6 J. M. Hutson, *Annu. Rev. Phys. Chem.*, 1990, **41**, 123–154.
7 K. B. Whaley, *Int. Rev. Phys. Chem.*, 1994, **13**, 41–84.
8 A. G. Császár, T. Szidarovszky, O. Asvany and S. Schlemmer, *Mol. Phys.*, 2019, **117**, 1559–1583.
9 F. Grandinetti, *Int. J. Mass Spectrom.*, 2004, **237**, 243–267.
10 E. J. Bieske and O. Dopfer, *Chem. Rev.*, 2000, **100**, 3963–3998.
11 F. Marinetti, E. Bodo and F. A. Gianturco, *ChemPhysChem*, 2007, **8**, 93–100.
12 N. Kobayashi, T. Kojima and Y. Kaneko, *J. Phys. Soc. Jpn.*, 1988, **57**, 1528–1531.
13 T. M. Kojima, N. Kobayashi and Y. Kaneko, *Z. Phys. D*, 1992, **23**, 181–185.
14 H. Tanuma, J. Sanderson and N. Kobayashi, *J. Phys. Soc. Jpn.*, 1999, **68**, 2570–2575.
15 O. Dopfer, *Int. Rev. Phys. Chem.*, 2003, **22**, 437–495.
16 O. Dopfer, *Z. Phys. Chem.*, 2005, **219**, 125–168.
17 E. J. Bieske, A. S. Soliva, A. Friedmann and J. P. Maier, *J. Chem. Phys.*, 1992, **96**, 28–34.
18 S. A. Nizkorodov, J. P. Maier and E. J. Bieske, *J. Chem. Phys.*, 1995, **103**, 1297–1302.
19 M. Meuwly, S. A. Nizkorodov, J. P. Maier and E. J. Bieske, *J. Chem. Phys.*, 1996, **104**, 3876–3885.
20 O. Dopfer, D. Roth and J. P. Maier, *Chem. Phys. Lett.*, 1999, **310**, 201.
21 O. Dopfer, S. A. Nizkorodov, M. Meuwly, E. J. Bieske and J. P. Maier, *Chem. Phys. Lett.*, 1996, **260**, 545–550.
22 N. M. Lakin, R. V. Olkhov and O. Dopfer, *Faraday Discuss.*, 2001, **118**, 455.
23 D. Roth, S. A. Nizkorodov, J. P. Maier and O. Dopfer, *J. Chem. Phys.*, 1998, **109**, 3841–3849.
24 D. Roth, O. Dopfer and J. P. Maier, *Phys. Chem. Chem. Phys.*, 2001, **3**, 2400.
25 S. A. Nizkorodov, D. Roth, R. V. Olkhov, J. P. Maier and O. Dopfer, *Chem. Phys. Lett.*, 1997, **278**, 26–30.
26 R. V. Olkhov, S. A. Nizkorodov and O. Dopfer, *J. Chem. Phys.*, 1999, **110**, 9527.
27 O. Dopfer and D. Luckhaus, *J. Chem. Phys.*, 2002, **116**, 1012.
28 R. V. Olkhov and O. Dopfer, *Chem. Phys. Lett.*, 1999, **314**, 215–222.
29 N. Solcà and O. Dopfer, *J. Phys. Chem. A*, 2001, **105**, 5637–5645.
30 M. Schmies, A. Patzer, M. Schütz, M. Miyazaki, M. Fujii and O. Dopfer, *Phys. Chem. Chem. Phys.*, 2014, **16**, 7980–7995.
31 A. Patzer, M. Schütz, T. Möller and O. Dopfer, *Angew. Chem., Int. Ed.*, 2012, **51**, 4925–4929.
32 M. Brümmer, C. Kaposta, G. Santambrogio and K. R. Asmis, *J. Chem. Phys.*, 2003, **119**, 12700–12703.
33 K. R. Asmis and J. Sauer, *Mass Spectrom. Rev.*, 2007, **26**, 542–562.
34 O. Asvany, S. Brünken, L. Kluge and S. Schlemmer, *Appl. Phys. B*, 2014, **114**, 203–211.
35 C. J. Johnson, A. B. Wolk, J. A. Fournier, E. N. Sullivan, G. H. Weddle and M. A. Johnson, *J. Chem. Phys.*, 2014, **140**, 221101.
36 D. Gerlich, *J. Chin. Chem. Soc.*, 2018, **65**, 637–653.
37 I. Savić, D. Gerlich, O. Asvany, P. Jusko and S. Schlemmer, *Mol. Phys.*, 2015, **113**, 2320–2332.
38 J. Roithova, A. Gray, E. Andris, J. Jasik and D. Gerlich, *Acc. Chem. Res.*, 2016, **49**, 223–230.
39 O. Boyarkin, *Int. Rev. Phys. Chem.*, 2018, **37**, 559–606.
40 P. J. Kelleher, C. J. Johnson, J. A. Fournier, M. A. Johnson and A. B. McCoy, *J. Phys. Chem. A*, 2015, **119**, 4170–4176.
41 T. Salomon, M. Töpfer, P. Schreier, S. Schlemmer, H. Kohguchi, L. Surin and O. Asvany, *Phys. Chem. Chem. Phys.*, 2019, **21**, 3440–3445.
42 M. Töpfer, T. Salomon, H. Kohguchi, O. Dopfer, K. M. T. Yamada, S. Schlemmer and O. Asvany, *Phys. Rev. Lett.*, 2018, **121**, 143001.
43 P. Jusko, S. Brünken, O. Asvany, S. Thorwirth, A. Stoffels, L. van der Meer, G. Berden, B. Redlich, J. Oomens and S. Schlemmer, *Faraday Discuss.*, 2019, **217**, 172–202.
44 O. Asvany and S. Schlemmer, *Phys. Chem. Chem. Phys.*, 2021, **23**, 26602–26622.
45 M. Töpfer, A. Jensen, K. Nagamori, H. Kohguchi, T. Szidarovszky, A. G. Császár, S. Schlemmer and O. Asvany, *Phys. Chem. Chem. Phys.*, 2020, **22**, 22885–22888.
46 J. A. Davies, N. A. Besley, S. Yang and A. M. Ellis, *J. Chem. Phys.*, 2019, **151**, 194307.
47 E. K. Campbell, M. Holz, D. Gerlich and J. P. Maier, *Nature*, 2015, **523**, 322–323.
48 D. Gerlich, J. Jašík and J. Roithová, *Int. J. Mass Spectrom.*, 2019, **438**, 78–86.
49 D. Gerlich, J. Jasik, V. D. Strelnikov and J. Roithova, *Astrophys. J.*, 2018, **864**, 62.
50 C. A. Rice, F. X. Hardy, O. Gause and J. P. Maier, *J. Phys. Chem. Lett.*, 2014, **5**, 942–945.
51 T. Gonzalez-Lezana, O. Echt, M. Gatchell, M. Bartolomei, J. Campos-Martinez and P. Scheier, *Int. Rev. Phys. Chem.*, 2020, **39**, 465–516.
52 A. Mauracher, O. Echt, A. M. Ellis, S. Yang, D. K. Bohme, J. Postler, A. Kaiser, S. Denifl and P. Scheier, *Phys. Rep.*, 2018, **751**, 1–90.
53 L. Kranabetter, N. K. Bersenkowitsch, P. Martini, M. Gatchell, M. Kuhn, F. Laimer, A. Schiller, M. K. Beyer, M. Ončák and P. Scheier, *Phys. Chem. Chem. Phys.*, 2019, **21**, 25362–25368.
54 C. Leidlmair, Y. Wang, P. Bartl, H. Schöbel, S. Denifl, M. Probst, M. Alcamí, F. Martín, H. Zettergren, K. Hansen, O. Echt and P. Scheier, *Phys. Rev. Lett.*, 2012, **108**, 076101.

 This journal is © the Owner Societies 2022

Open Access Article. Published on 20 April 2022. Downloaded on 12/31/2025 2:24:13 PM.
This article is licensed under a Creative Commons Attribution 3.0 Unported Licence.

55 A. Schiller, M. Meyer, P. Martini, F. Zappa, S. A. Krasnokutski, F. Calvo and P. Scheier, *J. Phys. Chem. A*, 2021, **125**, 7813–7824.
56 M. Meyer, P. Martini, A. Schiller, F. Zappa, S. A. Krasnokutski and P. Scheier, *Astrophys. J.*, 2021, **913**, 136.
57 M. Gatchell, P. Martini, F. Laimer, M. Goulart, F. Calvo and P. Scheier, *Faraday Discuss.*, 2019, **217**, 276–289.
58 S. Spieler, M. Kuhn, J. Postler, M. Simpson, R. Wester, P. Scheier, W. Ubachs, X. Bacalla, J. Bouwman and H. Linnartz, *Astrophys. J.*, 2017, **846**, 6.
59 N. B. Brauer, S. Smolarek, X. Zhang, W. J. Buma and M. Drabbels, *J. Phys. Chem. Lett.*, 2011, **2**, 1563–1566.
60 D. A. Thomas, E. Mucha, S. Gewinner, W. Schöllkopf, G. Meijer and G. von Helden, *J. Phys. Chem. Lett.*, 2018, **9**, 2305–2310.
61 X. Zhang, N. B. Brauer, G. Berden, A. M. Rijs and M. Drabbels, *J. Chem. Phys.*, 2012, **136**, 044305.
62 F. Bierau, P. Kupser, G. Meijer and G. von Helden, *Phys. Rev. Lett.*, 2010, **105**, 133402.
63 E. Mucha, A. I. González Flórez, M. Marianski, D. A. Thomas, W. Hoffmann, W. B. Struwe, H. S. Hahm, S. Gewinner, W. Schöllkopf, P. H. Seeberger, G. von Helden and K. Pagel, *Angew. Chem., Int. Ed.*, 2017, **56**, 11248–11251.
64 S. Erukala, A. Feinberg, A. Singh and A. F. Vilesov, *J. Chem. Phys.*, 2021, **155**, 084306.
65 D. Verma, S. Erukala and A. F. Vilesov, *J. Phys. Chem. A*, 2020, **124**, 6207–6213.
66 S. Erukala, D. Verma and A. Vilesov, *J. Phys. Chem. Lett.*, 2021, **12**, 5105–5109.
67 J. A. Davies, S. Yang and A. M. Ellis, *Phys. Chem. Chem. Phys.*, 2021, **23**, 27449–27459.
68 A. Günther, P. Nieto, D. Müller, A. Sheldrick, D. Gerlich and O. Dopfer, *J. Mol. Spectrosc.*, 2017, **332**, 8–15.
69 F. Wyrowski, K. M. Menten, R. Güsten and A. Belloche, *Astron. Astrophys.*, 2010, **518**, A26.
70 V. Ossenkopf, *et al.*, *Astron. Astrophys.*, 2010, **518**, L111.
71 J. M. Hollis, E. B. Churchwell, E. Herbst and F. C. De Lucia, *Nature*, 1986, **322**, 524–526.
72 A. Das, M. Sil, B. Bhat, P. Gorai, S. K. Chakrabarti and P. Caselli, *Astrophys. J.*, 2020, **902**, 131.
73 P. B. Crandall, D. Müller, J. Leroux, M. Förstel and O. Dopfer, *Astrophys. J.*, 2020, **900**, L20.
74 P. Nieto, D. Müller, A. Sheldrick, A. Günther, M. Miyazaki and O. Dopfer, *Phys. Chem. Chem. Phys.*, 2018, **20**, 22148–22158.
75 D. Müller and O. Dopfer, *J. Photochem. Photobiol.*, 2020, **3–4**, 100009.
76 D. Müller and O. Dopfer, *J. Phys. Chem. A*, 2021, **125**, 3146–3158.
77 M. Töpfer, P. C. Schmid, H. Kohguchi, K. M. T. Yamada, S. Schlemmer and O. Asvany, *Mol. Phys.*, 2019, **117**, 1481–1485.
78 R. V. Olkhov, S. A. Nizkorodov and O. Dopfer, *J. Chem. Phys.*, 1998, **108**, 10046–10060.
79 O. Dopfer, R. V. Olkhov and J. P. Maier, *J. Chem. Phys.*, 2000, **112**, 2176.
80 M. J. Frisch, *et al.*, *Gaussian16, Rev. C.01*, Gaussian, Inc., Wallingford, CT, 2016.
81 R. A. Aziz, F. R. W. McCourt and C. C. K. Wong, *Mol. Phys.*, 1987, **61**, 1487–1511.
82 T. R. Huet, C. J. Pursell, W. C. Ho, B. M. Dinelli and T. Oka, *J. Chem. Phys.*, 1992, **97**, 5977.
83 O. Dopfer, D. Roth and J. P. Maier, *J. Chem. Phys.*, 2001, **114**, 7081.
84 O. Dopfer, *J. Phys. Chem. A*, 2000, **104**, 11693–11701.
85 O. Dopfer and V. Engel, *J. Chem. Phys.*, 2004, **121**, 12345.
86 X. Chen and M. Thachuk, *Int. J. Quant. Chem.*, 2005, **101**, 1–7.
87 J. P. Wagner, D. C. McDonald and M. A. Duncan, *J. Chem. Phys.*, 2017, **147**, 7.
88 H. Zhou, R. Yang, X. Jin and M. Zhou, *J. Phys. Chem. A*, 2005, **109**, 6003–6007.
89 G. E. Lopez, *J. Comput. Chem.*, 1995, **16**, 768–776.
90 P. J. Linstrom and W. G. Mallard, *NIST Chemistry WebBook*, NIST Standards and Technology, Gaithersburg MD, 20899, 2001, **https://webbook.nist.gov/**.
91 D. F. Liu, T. Wyttenbach and M. T. Bowers, *Int. J. Mass Spectrom.*, 2004, **236**, 81–90.
92 H. S. Kim, C. H. Kuo and M. T. Bowers, *J. Chem. Phys.*, 1990, **93**, 5594–5604.
93 O. Dopfer, D. Roth and J. P. Maier, *J. Phys. Chem. A*, 2000, **104**, 11702–11713.
94 J.-M. Liu, T. Nishigori, T. Maeyama, Q.-R. Huang, M. Katada, J.-L. Kuo and A. Fujii, *J. Phys. Chem. Lett.*, 2021, **12**, 7997–8002.
95 J. Tang and T. Oka, *J. Mol. Spectrosc.*, 1999, **196**, 120–130.
96 M. H. Begemann and R. J. Saykally, *J. Chem. Phys.*, 1985, **82**, 3570–3579.
97 S. Borocci, P. Cecchi, M. Giordani and F. Grandinetti, *Eur. J. Mass Spectrom.*, 2015, **21**, 171–181.
98 H. El Hanini, F. Najar, M. Naouai and N.-E. Jaidane, *Phys. Chem. Chem. Phys.*, 2019, **21**, 11705–11713.
99 J.-W. Li, M. Morita, K. Takahashi and J.-L. Kuo, *J. Phys. Chem. A*, 2015, **119**, 10887–10892.
100 A. B. McCoy, T. L. Guasco, C. M. Leavitt, S. G. Olesen and M. A. Johnson, *Phys. Chem. Chem. Phys.*, 2012, **14**, 7205–7214.
101 J. A. Tan, J.-W. Li, C.-C. Chiu, H.-Y. Liao, H. T. Huynh and J.-L. Kuo, *Phys. Chem. Chem. Phys.*, 2016, **18**, 30721–30732.
102 Q.-R. Huang, T. Nishigori, M. Katada, A. Fujii and J.-L. Kuo, *Phys. Chem. Chem. Phys.*, 2018, **20**, 13836–13844.
103 B. Bandyopadhyay, T. C. Cheng and M. A. Duncan, *Int. J. Mass Spectrom.*, 2010, **297**, 124–130.
104 J. Yang, X. Kong and L. Jiang, *Chem. Phys.*, 2018, **501**, 1–7.
105 K. Chatterjee and O. Dopfer, *Astrophys. J.*, 2020, **898**, 92.
106 E. P. L. Hunter and S. G. Lias, *J. Phys. Chem. Ref. Data*, 1998, **27**, 413–656.
107 H. Lew, *Can. J. Phys.*, 1976, **54**, 2028–2049.